RESEARCH ARTICLE

ADVANCED OPTICAL MATERIALS
www.advopticalmat.de

Secondary Coordination Sphere-Directed Design of Thermo-Responsive and Bright Luminescent Manganese(II) Complexes

Masaki Yoshida, Fuwenhan Zhang, Kaito Segawa, Kanon Komoda, Kodai Yuasa, Hiromu Obata, Nobuto Yoshinari, and Masako Kato**

Luminescent Mn^{II} complexes have attracted considerable attention as low-cost and earth-abundant alternatives to precious metal-based emitters. However, their development is limited by certain challenges, including severe thermal quenching, moisture sensitivity, and a lack of efficient strategies for generating stimuli-responsive luminescence. In this study, these issues are addressed by decorating the secondary coordination sphere of Mn^{II} complexes, thereby enhancing their emission efficiency and stimuli-responsive behavior. These Mn^{II} complexes can be easily synthesized by manual mechanochemical reactions. Among them, the bulkiness-introduced complexes $[MnBr_2\{OP(o\text{-Tol})_3\}_2]$ (*o*-Tol = *o*-tolyl) and $[MnBr_2\{OP(o\text{-An})_3\}_2]$ (*o*-An = *o*-anisyl) exhibit high emission quantum yields of 0.86 and 0.78, respectively. Furthermore, $[MnBr_2\{OP(o\text{-An})_3\}_2]$ exhibits thermochromic luminescence owing to excited-state interactions between the Mn^{II} center and the O atom of the methoxy group in the secondary coordination sphere. The results of this study confirm the potential of secondary coordination-sphere engineering as an effective strategy for optimizing Mn^{II} luminescence, thereby offering new design principles for stimuli-responsive photofunctional materials.

1. Introduction

The development of luminescent complexes based on earth-abundant first-row transition metals has emerged as a promising strategy for sustainable optoelectronic materials,[1,2] and as alternatives to precious metal-based materials. Among these, luminescent Mn^{II} complexes are particularly interesting because of the abundance and low cost of Mn resources, and their unique photophysical properties.[2] The paradigmatic complex $[MnBr_2(OPPh_3)_2]$ ($OPPh_3$ = triphenylphosphine oxide) reported in 1961 exhibits luminescence originating from a metal-centered d–d ($^4T_1(G) \rightarrow {}^6A_1$) excited state.[3] After their discovery, this class of compounds remained relatively unexplored for decades. Recently, owing to renewed interest in luminescent Mn^{II} complexes, these compounds are being utilized in organic light-emitting diodes and X-ray scintillators.[4,5] These luminescent Mn^{II} complexes can be mainly classified into two types:[2] (i) neutral or cationic Mn^{II} complexes with phosphine oxide ligands, and (ii) salts composed of anionic $[Mn^{II}X_4]^{2-}$ (X^- = Cl^-, Br^-, and I^-) species and cations. Among these, phosphine oxide-based complexes are particularly attractive because their coordination environment and ligand field can be more readily tuned by modifying the ligand structure, allowing better control of the photophysical properties.

However, luminescent Mn^{II} complexes are associated with some fundamental problems that require resolution.[2] First, Mn^{II} complexes exhibit significant deformation in the d–d excited state, resulting in nonradiative deactivation. In addition, they are sometimes sensitive to moisture, which results in emission quenching. Despite several attempts,[6,7] designing luminescent Mn^{II} complexes that are not limited by the above-mentioned issues remains challenging. Furthermore, in contrast to numerous reports on the chromic luminescence of various first-row transition metal complexes, such as Cu^I complexes,[1b,g] rational molecular design strategies that enable Mn^{II} complexes to exhibit stimuli-responsive emission color changes (i.e., chromic luminescence) have not yet been established. In addition, the synthesis of most luminescent Mn^{II} complexes, typically involving

M. Yoshida, F. Zhang, K. Segawa, K. Komoda, K. Yuasa, H. Obata, M. Kato
Department of Applied Chemistry for Environment
School of Biological and Environmental Sciences
Kwansei Gakuin University
1 Gakuen-Uegahara, Sanda, Hyogo 669–1330, Japan
E-mail: myoshida@chem.sci.osaka-u.ac.jp; katom@kwansei.ac.jp

M. Yoshida, N. Yoshinari
Department of Chemistry, Graduate School of Science
The University of Osaka
1-1 Machikaneyama, Toyonaka, Osaka 560-0043, Japan

F. Zhang
Institute of Industrial Science
The University of Tokyo
4-6-1 Komaba, Meguro-ku, Tokyo 153–8505, Japan

K. Segawa
Department of Chemistry
Faculty of Science
Kyushu University
744 Motooka, Nishi-ku, Fukuoka 819-0395, Japan

The ORCID identification number(s) for the author(s) of this article can be found under https://doi.org/10.1002/adom.202502008

DOI: 10.1002/adom.202502008

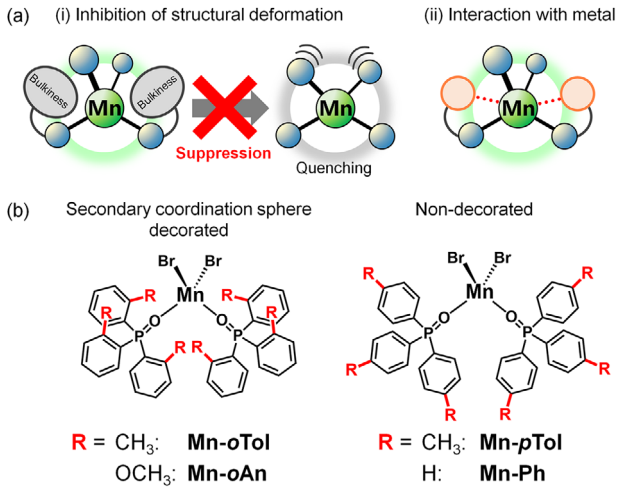

Scheme 1. a) Schematics of functional-group introduction into the secondary coordination sphere of Mn^{II} complexes. b) Structural formulas of the Mn^{II} complexes synthesized in this study.

excess organic solvents and long durations (several hours to days), is time-consuming and eco-unfriendly.

Herein, we report a design paradigm based on secondary coordination-sphere engineering in which steric and electronic functionalities are introduced around an Mn^{II} center via phosphine oxide ligands (**Scheme** 1a). Among the many recent reports on luminescent Mn^{II} complexes, most molecular designs have been approached from the perspective of inorganic material chemistry, and organic ligands are mainly considered as light-harvesting antennas or separators inhibiting Mn···Mn interactions. In contrast, from the viewpoint of coordination chemistry, the introduction of functional groups around the secondary coordination sphere is expected to improve the photophysical properties of Mn^{II} complexes. Besides suppressing the quenching of excited states due to bulkiness ((i) in Scheme 1a),[6e] this strategy controls chromic phenomena by modulating interactions with the Mn^{II} ion ((ii) in Scheme 1(a)). For this purpose, we have focused on $[MnBr_2\{OP(o\text{-}Tol)_3\}_2]$[8] and $[MnBr_2\{OP(o\text{-}An)_3\}_2]$ (**Mn-*o*Tol** and **Mn-*o*An**, respectively, in Scheme 1(b); *o*Tol = *o*-tolyl, *o*An = *o*-anisyl) in which the secondary coordination sphere of $[MnBr_2(OPPh_3)_2]$ (**Mn-Ph** in Scheme 1b) was modified. In addition, $[MnBr_2\{OP(p\text{-}Tol)_3\}_2]$ (**Mn-*p*Tol** in Scheme 1(b); *p*-Tol = *p*-tolyl) is synthesized to compare the effects of the secondary coordination sphere. In this study, the bulkiness-introduced **Mn-*o*Tol** and **Mn-*o*An** complexes exhibited extremely bright luminescence with emission quantum yields of 0.86 and 0.78, respectively. Furthermore, **Mn-*o*An** exhibited significant thermochromic luminescence driven by intramolecular Mn···O interactions. This study reports the first mechanochemical synthesis of neutral luminescent Mn^{II} complexes, providing a rapid and solvent-minimized alternative to traditional solution-phase methods.[9,10] The results of this study confirm that secondary coordination-sphere modification is a promising strategy for advancing Mn^{II}-based photofunctional materials.

2. Results and Discussion

2.1. Mechanochemical Synthesis

First, we attempted the mechanochemical synthesis of **Mn-*o*Tol**, in which methyl groups were introduced into the secondary coordination sphere of the Mn^{II} center, although a solution-state synthesis for this compound has been previously reported.[8] As shown in **Figure** 1, the manual grinding of $MnBr_2$ and two equivalents of $OP(o\text{-}Tol)_3$ in the presence of a few drops of EtOH immediately yields a strongly green-emissive powder under UV light. Here, the progress of the reaction was monitored visually by observing the disappearance of starting materials. The powder X-ray diffraction (PXRD) pattern of the resulting solid (**Figure** 2a) is consistent with the pattern simulated from the crystal structure of **Mn-*o*Tol**[8] (**Figure** 3a), confirming the successful formation of the target compound, **Mn-*o*Tol**. This reaction also proceeded smoothly when $MnBr_2{\cdot}4H_2O$ was used (Figure S1a, Supporting Information) instead of anhydrous $MnBr_2$. Similarly, **Mn-*p*Tol** and **Mn-Ph**,[3] which lack bulky substituents in the secondary coordination sphere, could also be synthesized by the same mechanochemical method (Figure 2b,c). The structure of the newly synthesized complex **Mn-*p*Tol** was investigated by X-ray crystallography (Figure 3b), and the purity of the synthesized complexes was confirmed by elemental analysis (see Experimental Section). Thus, we have concluded that these Mn^{II} complexes were successfully synthesized by a simple mechanochemical method, which is faster than conventional solution reactions.

Subsequently, **Mn-*o*An**, with bulky methoxy groups in the secondary coordination sphere at the Mn^{II} center, was attempted to synthesize. Although $MnBr_2$ and $OP(o\text{-}An)_3$ are soluble in EtOH, no reaction occurs when $MnBr_2$ and $OP(o\text{-}An)_3$ are ground with a few drops of EtOH (Figure S1b, Supporting Information). Furthermore, even when using the conventional solution-state reaction, **Mn-*o*An** could not be obtained in EtOH, resulting in ligand decomposition. In contrast, the manual grinding of $MnBr_2$ and $OP(o\text{-}An)_3$ with a few drops of acetone yields a weakly green-emissive powder ((i) in **Figure** 4a). After successive grinding of this powder with a few drops of EtOH for a few minutes initially yields a yellow-green luminescent powder ((ii) in Figure 4a),

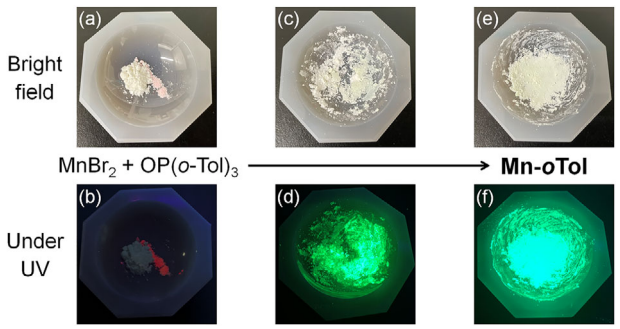

Figure 1. Bright field (a,c,e) and luminescence (b,d,f) images showing the synthesis of **Mn-*o*Tol** by the proposed mechanochemical reaction: (a,b) mixture of $MnBr_2$ and $OP(o\text{-}Tol)_3$ (c,d) immediately after beginning to grind the mixture with 1 drop of EtOH and (e,f) after 5 min of grinding with an additional drop of EtOH.

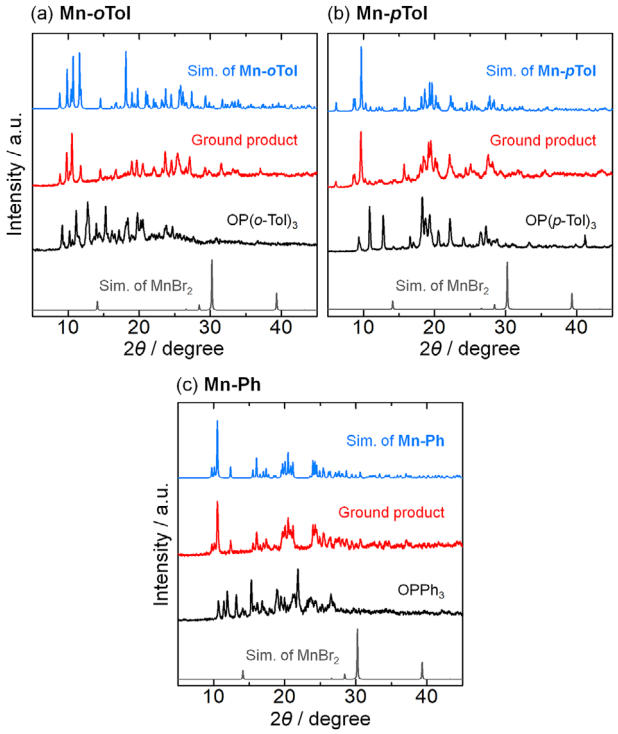

Figure 2. PXRD patterns of a) **Mn-*o*Tol**, b) **Mn-*p*Tol**, and c) **Mn-Ph** synthesized by the mechanochemical method (red lines) and those of the corresponding free ligands (black lines). Gray and blue lines indicate the PXRD patterns simulated from the crystal structures of $MnBr_2$[11] (gray) and Mn^{II} complexes (blue).

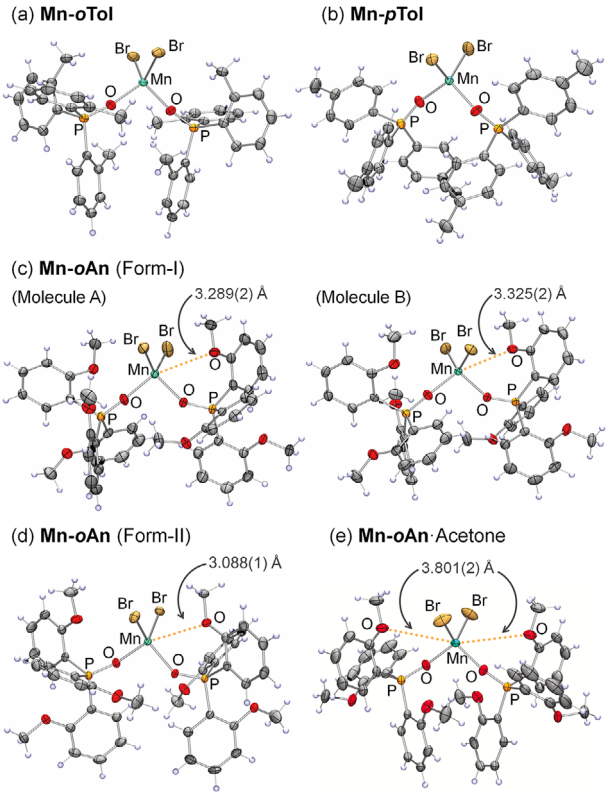

Figure 3. Molecular structures of a) **Mn-*o*Tol**, b) **Mn-*p*Tol**, and c-e) **Mn-*o*An** [(c) Form-I (A and B indicate two crystallographically independent molecules), (d) Form-II, and (e) **Mn-*o*An**·acetone] at 150 K. The thermal ellipsoids are displayed at the 50% probability level. The acetone molecule is omitted for clarity. Orange dotted lines indicate the closest Mn···O(methoxy) distances.

which transforms into a green luminescent powder on heavy grinding for 15 min ((iii) in Figure 4a).

The formation of the target compound **Mn-*o*An** by the mechanochemical reaction is confirmed by the PXRD patterns (Figure 4b) and X-ray crystallographic analysis of the recrystallized samples (Figure 3c–e). In contrast to **Mn-*o*Tol** and **Mn-*p*Tol**, two crystal polymorphs and one acetone-solvated form can be isolated for **Mn-*o*An**. Among them, the two polymorphs (Form-I and Form-II) are obtained by recrystallization from $EtOH/Et_2O$; Form-I (Figure 3c) crystallizes preferentially from the (super)saturated solution within a few hours, whereas Form-II (Figure 3d) grows gradually over several days in a refrigerator. Therefore, Form-I and Form-II are considered to be kinetic and thermodynamically stable crystals, respectively.[12] Indeed, the Form-I crystals gradually transform into Form-II crystals in solution (Figure S3, Supporting Information), and the crystal density of Form-II (1.505 g cm^{-3}) is higher than that of Form-I (1.490 g cm^{-3}). In addition, acetone-solvated crystals (**Mn-*o*An**·acetone; Figure 3e; Figure S2, Supporting Information) are directly obtained from a suspension containing $MnBr_2$ and OP(*o*-An)$_3$ in acetone (see Experimental Section). Notably, the PXRD patterns of the samples in which the starting materials are ground with acetone ((i) in Figure 4b) and then with EtOH ((ii) in Figure 4b) are in agreement with the patterns simulated from the single crystal structures of **Mn-*o*An**·acetone and Form-I of **Mn-*o*An**, respectively. Although the crystallinity decreases, the pattern of the more heavily ground sample ((iii) in Figure 4b) is

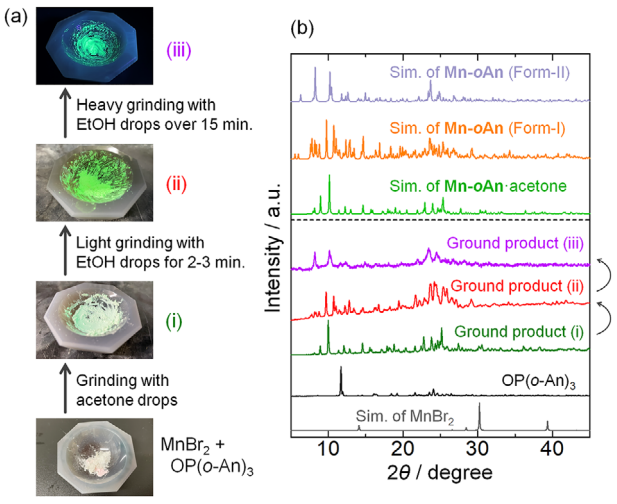

Figure 4. a) Photographs of the mechanochemical synthesis of **Mn-*o*An** under UV light. b) PXRD patterns of the mechanochemically synthesized sample after grinding with (i) acetone (green line) followed by (ii) light and (iii) heavy grinding with EtOH (red and purple lines, respectively). The black line indicates the pattern of OP(*o*-An)$_3$, while the gray, pale green, orange, and pale purple lines indicate the patterns simulated from the crystal structures of $MnBr_2$ (gray), **Mn-*o*An**·acetone (pale green), and **Mn-*o*An** (Form-I: orange; Form-II: pale purple).

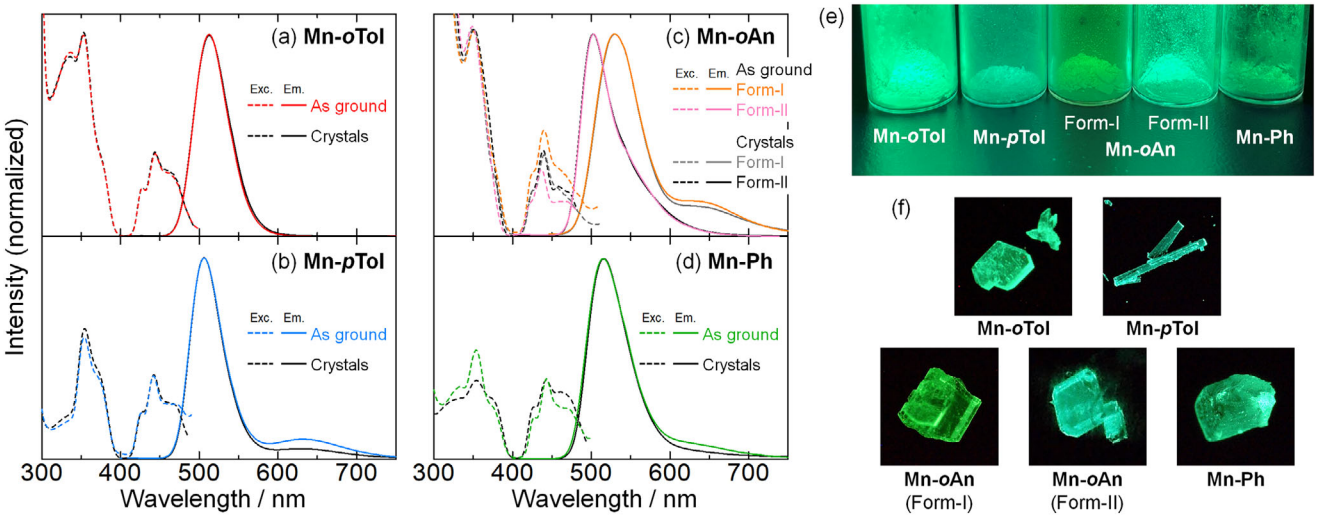

Figure 5. a–d) Emission (solid lines) and excitation (broken lines) spectra of mechanochemically synthesized (colored lines) and polycrystalline samples (black or gray lines) of (a) **Mn-*o*Tol**, (b) **Mn-*p*Tol**, (c) **Mn-*o*An**, and (d) **Mn-Ph** in the solid state at 293 K (λ_{ex} = 350 nm). Gray lines in (c) indicate the emission and excitation spectra of Form-II of **Mn-*o*An**. Excitation spectra are measured using each emission maximum wavelength as the detection wavelength. e,f) Photographs of the (e) mechanochemically synthesized powders and (f) crystals of complexes under UV light.

consistent with the simulated pattern for Form-II of **Mn-*o*An**. Notably, elemental analysis confirmed the synthesis of **Mn-*o*An** by the mechanochemical method further (see Experimental Section). Because **Mn-*o*An** is poorly soluble in acetone, the use of acetone likely suppresses the reverse reaction (dissociation) and side reactions due to the bulkiness of the ligand, resulting in efficient synthesis in acetone. Upon grinding with EtOH (Figure 4b) or soaking in AcOEt (Figure S3, Supporting Information), **Mn-*o*An**·acetone first transforms into Form-I (the kinetic product), which subsequently converts into the thermodynamically stable Form-II.

Notably, all previous studies on the mechanochemical synthesis of luminescent Mn^{II} complexes report for organic–inorganic hybrid Mn^{II} halides with the general formula $A_n[MnX_m]$ (A = organic cations, X = Cl^-, Br^-, and I^-).[13] To the best of our knowledge, this is the first report of the mechanochemical synthesis of neutral luminescent Mn^{II} complexes.

2.2. Crystal Structures

As shown in Figure 3, the Mn^{II} ions in all complexes adopt a typical four-coordinate tetrahedral geometry coordinated by two bromide anions and two oxygen atoms of phosphine oxide. To discuss the distortion from ideal tetrahedral geometry, the dihedral angles between the O—Mn—O and Br—Mn–Br planes were compared (Figure S4; Table S2, Supporting Information). The dihedral angle of **Mn-*p*Tol** (89.61(4)°) is close to the ideal value of 90°, indicating that the geometry of **Mn-*p*Tol** is close to the ideal tetrahedral coordination geometry. In contrast, the dihedral angle of one of the crystallographically independent molecules of Form-I of **Mn-*o*An** (81.54(4)°) deviates from 90°, indicating significant distortion from the ideal tetrahedron. Regarding the substituents, in **Mn-*o*Tol**, all three methyl groups in OP(*o*-Tol)$_3$ are positioned on the same side as P═O, whereas in **Mn-*o*An**, one of the three methoxy groups in OP(*o*-An)$_3$ is flipped to the opposite side of P═O (Figure S5, Supporting Information), probably because of bulkiness. Importantly, short intramolecular Mn···O(methoxy) distances indicative of interactions between the Mn^{II} ion and the methoxy group located in the secondary coordination sphere are found in both Form-I and Form-II of **Mn-*o*An** (ca. 3.1–3.3 Å; Figure 3c,d). On the other hand, the Mn···O(methoxy) distance in **Mn-*o*An**·acetone (3.801(2) Å; Figure 3e) is longer than that in Form-I and Form-II. For all complexes, the closest Mn···Mn distance is beyond 9.5 Å (Table S2, Supporting Information), indicating the absence of Mn···Mn interactions or other special intermolecular interactions (Figure S6, Supporting Information). The absence of intermolecular Mn···Mn interactions and spin-state changes in each Mn^{II} center in the crystals is also confirmed by magnetic susceptibility measurements; the effective magnetic moments (μ_{eff} = 5.88 μ_B at 300 K for **Mn-*o*An** (Form-II)) (Figure S7, Supporting Information) are consistent with the spin-only value for the high-spin Mn^{II} complex with an $S = 5/2$ ground state (5.92 μ_B).

2.3. Emission Properties

Because all complexes showed green emission under UV light, their emission spectra were measured. As shown in **Figures 5** and S8 (Supporting Information), all the synthesized complexes exhibit a structureless intense emission band at ≈ 502–530 nm at 293 K, which can be attributed to the metal-centered d–d ($^4T_1(G) \rightarrow {}^6A_1$) transition typical of discrete tetrahedral Mn^{II} complexes.[2] Notably, these emission maxima are observed at lower energies than the phosphorescence bands originating from the triplet excited states of the free ligands,[14] further supporting that the emission is assignable to metal-centered rather than ligand-based luminescence. For **Mn-*o*Tol**, **Mn-*p*Tol**, and **Mn-Ph**, the emission and excitation spectra of the as-ground powders prepared by mechanochemical synthesis and the polycrystalline samples obtained by recrystallization are almost identical

Table 1. Photophysical data of the Mn^{II} complexes in the solid state under ambient air at 293 K.

	Mn-*o*Tol		Mn-*p*Tol		Mn-*o*An		Mn-*o*An ·acetone	Mn-Ph	
	As ground[a]	Crystals	As ground[a]	Crystals	As ground[a] (Form-I / Form-II)	Crystals (Form-I / Form-II)	Crystals	As ground[a]	Crystals
λ_{em}[b] / nm	512	513	506	507	530 / 503	530 / 502	509	515	516
Φ[c]	0.66[g]	0.86	0.06	0.09	0.08 / 0.47	0.09 / 0.78	0.03	0.05	0.22[g]
τ[d] / μs	611	575	115	130	203 / 1457	219 / 1403	182	125	211
k_r[e] / 10^3 s^{-1}	1.1	1.4	0.52	0.69	0.39 / 0.32	0.41 / 0.56	0.17	0.40	1.0
k_{nr}[f] / 10^3 s^{-1}	0.56	0.29	8.2	7.0	4.5 / 0.36	4.2 / 0.16	5.3	7.6	3.7

[a] Mechanochemically synthesized powder sample without recrystallization; [b] Emission maximum; [c] Emission quantum yield; [d] Emission lifetime; [e] Radiative rate constant, $k_r = \Phi/\tau_{av}$; [f] Nonradiative rate constant, $k_{nr} = k_r(1-\Phi)/\Phi$; [g] Consistent with the literature values (ref.[8] for **Mn-*o*Tol** and ref.[6a] for **Mn-Ph**).

(Figure 5a,b,d). For **Mn-*o*An**, the emission spectra of the lightly and heavily ground powders are almost consistent with the spectra of Form-I and Form-II, respectively (Figure 5c), in agreement with the PXRD results (Figure 4b). Moreover, the emission maximum wavelength (λ_{em}) shifts from 502 nm (Form-II of **Mn-*o*An**) to 506 nm (**Mn-*p*Tol**), 509 nm (**Mn-*o*An**·acetone), 513 nm (**Mn-*o*Tol**), 516 nm (**Mn-Ph**), and finally to 530 nm (Form-I of **Mn-*o*An**). This emission shift can be rationalized based on the dihedral angle between the O—Mn—O and Br—Mn—Br planes (Table S2, Supporting Information). When the dihedral angle is close to the ideal 90° (**Mn-*p*Tol**, Form-II of **Mn-*o*An**, and **Mn-*o*An**·acetone), the emission maximum appears at ≈505 nm, and at a dihedral angle of ≈85° (**Mn-*o*Tol** and **Mn-Ph**), the emission is observed at ≈515 nm. One of the crystallographically independent Form-I molecules of **Mn-*o*An** is significantly distorted (81.5° dihedral angle), and its emission band is significantly shifted (to 530 nm). Because the emission energy of Mn^{II} ions is sensitive to the ligand field symmetry and strength,[2,15,16] this emission shift could originate from the slightly increased ligand field strength due to distortion from the ideal tetrahedral geometry. In addition to this intense band, a weak emission band at 630 nm appears for **Mn-*p*Tol** and Form-I of **Mn-*o*An** (Figure 5b,d), as discussed next. The excitation spectra of all complexes contain two characteristic excitation bands. The lowest-energy band (≈420–500 nm) corresponds to transitions to the G-terms, i.e., $^6A_1 \rightarrow {}^4T_1(G)$, $^4T_2(G)$, $^4E(G)$, and $^4A_1$, while the second-lowest-energy band (≈310–400 nm) corresponds to transitions to the D-terms, i.e., $^6A_1 \rightarrow {}^4T_2(D)$ and $^4E(D)$.[2] These excitation bands are consistent with those observed in the UV–vis diffuse reflectance spectra (Figure S9a, Supporting Information). In addition, the intense absorption bands below 310 nm can be attributed to the $^1\pi\pi^*$ absorption of the phosphine oxide ligand (Figure S9b, Supporting Information).

Table 1 summarizes the photophysical data for the synthesized complexes. The emission quantum yield of the mechanochemically synthesized **Mn-*o*Tol** ($\Phi = 0.66$) reproduces the literature value ($\Phi = 0.63$),[8] while the well-crystalline sample of **Mn-*o*Tol** shows a higher quantum yield ($\Phi = 0.86$).[4,6,17] A similarly high emission quantum yield is observed for **Mn-*o*An** Form-II (Φ = 0.78). These values are notably high among neutral Mn^{II} complexes reported to date (Scheme S1). This result confirms that nonradiative decay can be effectively suppressed by introducing steric bulk[6e] around the Mn center through *ortho*-substituted phosphine oxides (Figure S10, Supporting Information), in contrast to the unsubstituted **Mn-Ph** ($\Phi = 0.22$). Of course, as reported previously,[7,8,17] the large Mn···Mn distances might also contribute toward their high emission quantum yields by suppressing quenching via Mn···Mn interactions. In contrast, the emission quantum yield of **Mn-*o*An** Form-I ($\Phi = 0.09$) is lower than that of **Mn-Ph** ($\Phi = 0.22$) and similar to that of **Mn-*p*Tol** ($\Phi = 0.09$). The significantly low emission efficiency of Form-I of **Mn-*o*An** can be attributed to loose molecular packing, as indicated by the low crystal density of the system (1.490 and 1.505 g cm^{-3} for Form-I and Form-II, respectively), which is likely insufficient to effectively suppress structural distortion in the excited state. Furthermore, as discussed in the next section, the relatively low emission quantum yields of **Mn-*p*Tol** and Form-I of **Mn-*o*An** can also be attributed to humidity. In addition to the emission quantum yields discussed above, all the complexes exhibit sub-millisecond-to-millisecond-order emission lifetimes, typical of the $^4T_1(G) \rightarrow {}^6A_1$ phosphorescence in Mn^{II} complexes.[2] Although **Mn-Ph** has been reported to exhibit triboluminescence (i.e., luminescence induced by mechanical stress without photoexcitation),[3] **Mn-*o*Tol**, **Mn-*p*Tol**, and **Mn-*o*An** do not show any observable triboluminescence in ambient air.

Next, the dependence of the emission behavior of the complexes on humidity was examined. The emission spectra of **Mn-*p*Tol** and Form-I of **Mn-*o*An** contain a weak emission band at ≈630 nm in addition to the main emission band. Notably, the intensity of this weak emission band increases at high values of relative humidity (RH) (**Figure 6**a,b). This emission band is typical of the $^4T_1(G) \rightarrow {}^6A_1$ transition in five- or six-coordinated ligand fields of Mn^{II} complexes,[2,16] suggesting that the Mn^{II} centers of **Mn-*p*Tol** and Form-I of **Mn-*o*An** are attacked by water molecules in humid conditions. In contrast, thermogravimetric analysis of **Mn-*p*Tol** and Form-I of **Mn-*o*An** stored in ambient air show negligible desorption (Figure S11, Supporting Information); therefore, the attack of water molecules occurs only on the surface of the crystals. In addition, the emission intensity increases on heating (Figure 6c,d; Figure S12a, Supporting Information), indicating that the low emission quantum yields of these complexes ($\Phi = 0.09$) can be attributed to quenching by water. Indeed, the emission intensity and lifetime of **Mn-*p*Tol** increases rapidly below 270 K, accompanied with the disappearance of the emission band at 630 nm (Figure S12, Supporting Information; see **Figure 7**b for **Mn-*o*An** Form-I). These results suggest that, at

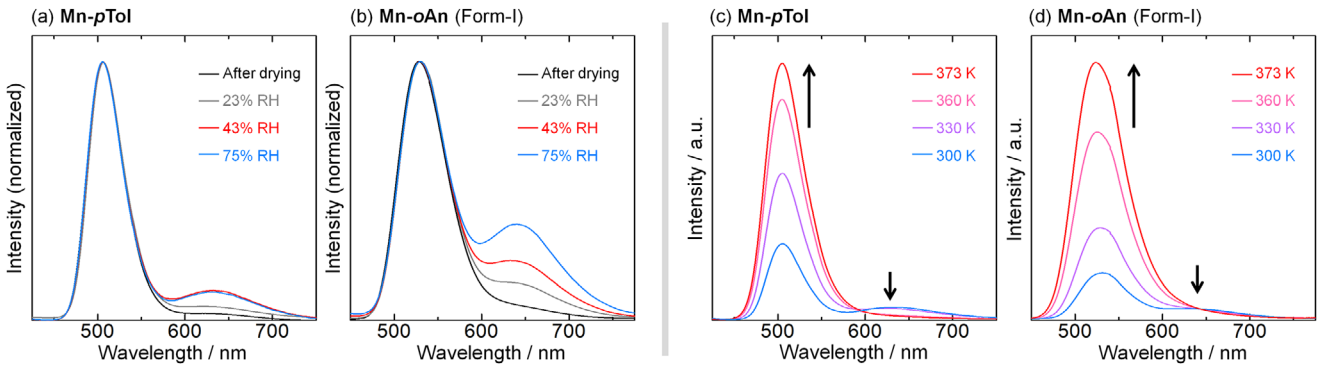

Figure 6. a,b) Emission spectra of (a) **Mn-*p*Tol** and (b) Form-I of **Mn-*o*An** (λ_{ex} = 350 nm) in the solid state at 293 K, after drying (black) and stored at 23% RH (grey), 43% RH (red), or 75% RH (blue) for 2 days. c,d) Variable-temperature emission spectra of (c) **Mn-*p*Tol** and (d) Form-I of **Mn-*o*An** in the solid state (λ_{ex} = 350 nm).

room temperature (ca. 293 K), a transient 5–6 coordinated intermediate is formed by the attack of water molecules on the Mn^{II} center during excitation, where the activation barrier is calculated to be 3.0×10^3 cm^{-1}, thereby weakening the emission. In contrast, no significant spectral changes are observed for **Mn-*o*Tol** and Form-II of **Mn-oAn**, even at 75% RH (Figure S13, Supporting Information). Thus, owing to a lower bulkiness and density (**Mn-*p*Tol** and **Mn-*o*Tol** crystals show a density of 1.408 and 1.456 g cm^{-3}, respectively), **Mn-*p*Tol** should be more easily attacked by water molecules than **Mn-*o*Tol**. Similarly, the difference in humidity response between the two polymorphs of **Mn-*o*An** can be explained by structural differences: the methoxy groups on the OP(*o*-An)$_3$ ligand are positioned closer to the Mn center in Form-II than in Form-I (Figure S10, Supporting Information), and the crystal density of Form-II (1.505 g cm^{-3}) is higher than that of Form-I (1.490 g cm^{-3}), which would hinder the attack of water molecules on the Mn center. The more significant change in emission with humidity for **Mn-*o*An** (Form-I) than for **Mn-*p*Tol** can be attributed to hydrogen bonding between the methoxy groups and water molecules. These observations suggest that differences in molecular packing and the spatial proximity of functional groups to the Mn center play important roles in determining the humidity sensitivity of the emission properties.

2.4. Thermochromic Behavior of Mn-oAn

Notably, both Form-I and Form-II of **Mn-*o*An** exhibit significant thermochromic luminescence. When the crystals of Form-II are cooled to 77 K, their emission changes from blue-green to yellow-green (Figure 7a; Figure S14, Supporting Information). Temperature dependence analysis indicates that the intensity of the emission band at 502 nm (termed the "HE (high-energy emission) band") decreases, while that of the shoulder band ≈555 nm (termed the "LE (low-energy emission) band") increases with decreasing temperature. After reheating to ambient temperature, the HE band intensity increases again, and the original emission spectrum is reversibly recovered (Figure S15, Supporting Information). Notably, the emission maximum energy of the LE band is red-shifted at low temperatures, whereas the temperature dependence of the HE band energy is not significant (Figure S16, Supporting Information). A similar change in emission color and the appearance of a new LE band at low temperatures are also observed for Form-I (Figure 7b); however, the intensity of the LE band of Form-I at 577 nm is significantly weaker than that of Form-II, and the HE band remains the main component of the spectrum, even at 77 K. In contrast, the d–d transition bands in the excitation spectra show no significant temperature dependence (Figure S17, Supporting Information), suggesting that the observed thermochromic luminescence originates from excited-state structural deformation. Furthermore, no crystal phase transition or change in magnetic susceptibility is observed within the measured temperature range (Figure S7; Table S1, Supporting Information), indicating that the thermochromism is primarily driven by *intra*molecular (rather than *inter*molecular) interactions. As **Mn-*o*Tol**, **Mn-*p*Tol**, and even **Mn-*o*An**·acetone do not show obvious thermochromic luminescence (Figures S8,S12, and S18, Supporting Information), the temperature-dependent behaviors observed in this study can be attributed to the short intramolecular Mn···O(methoxy) distances in Form-I and Form-II of **Mn-*o*An**. These results indicate that the closest methoxy group in the secondary coordination sphere transiently coordinates with the Mn^{II} center in the excited state, thereby strengthening the ligand field via the formation of a transient pentacoordinate-like geometry. According to the Tanabe–Sugano diagram for d^5 systems,[2] the energy of the $^4T_1(G) \rightarrow {}^6A_1$ transition decreases with increasing ligand field strength, leading to the appearance of a new emission band at lower energy.

To further investigate the origin of this thermochromic luminescence, the crystal structures of **Mn-*o*An** at 150 and 293 K were compared (Figure S19, Supporting Information). The closest intramolecular Mn···O(methoxy) distance in Form-II is found to elongate from 3.088(1) Å to 3.153(2) Å (Figure 7c), whereas the other distances do not change significantly (Table S2, Supporting Information). This finding suggests that the thermochromic luminescence observed here arises from temperature-dependent changes in the stability of transient Mn···O(methoxy)-coordinated species in the excited state, which shift the population distribution between the HE and LE emissive states (Figure 7d; see also Figure S20, Supporting Information).

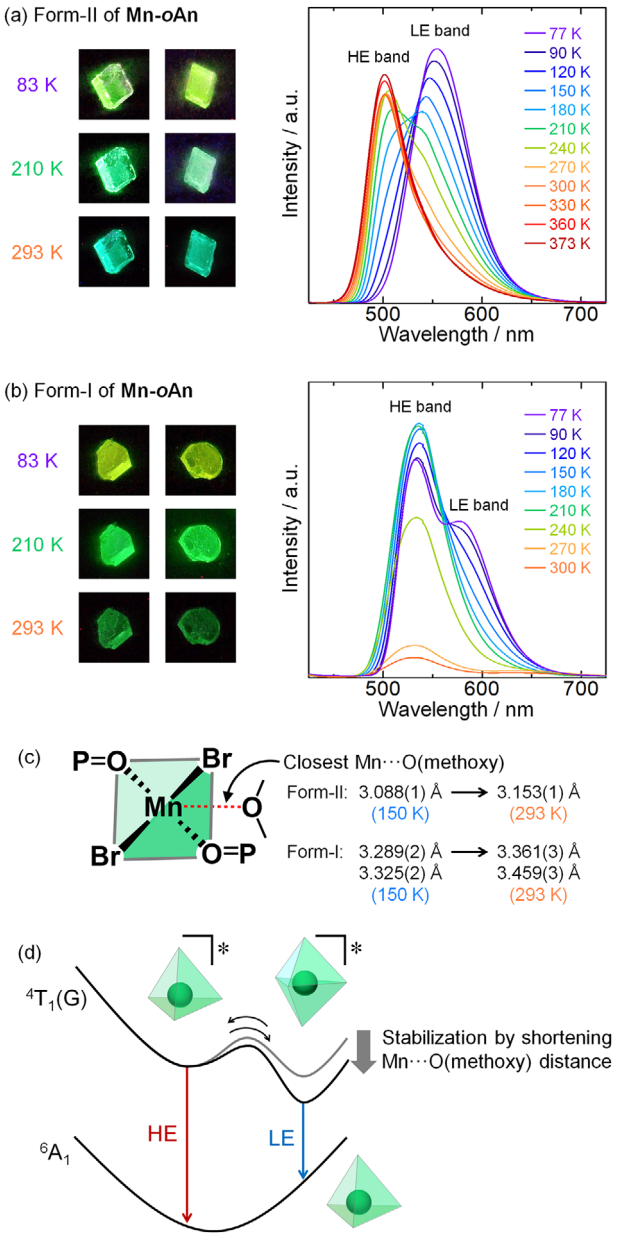

Figure 7. a,b) Variable-temperature microscopic photographs and emission spectra of (a) Form-II and (b) Form-I of **Mn-*o*An** in the solid state (λ_{ex} = 350 nm). c) Temperature-dependence of the closest Mn···O(methoxy) distances of **Mn-*o*An**. d) Schematic energy diagram of **Mn-*o*An**.

Notably, the closest Mn···O(methoxy) distance in Form-II at 293 K (3.153(2) Å) is shorter than that in Form-I at 150 K (3.286(2) Å). This result is consistent with the previously mentioned spectral observations, which indicate that the HE band remains the main component at 77 K in the spectrum of Form-I, whereas the LE band is still observed as a shoulder in the spectrum of Form-II at 373 K (Figure S16, Supporting Information). Overall, the introduction of methoxy groups into the secondary coordination sphere enables **Mn-*o*An** to exhibit thermochromic luminescence due to intramolecular Mn···O(methoxy) interactions in the excited state.

3. Conclusion

In conclusion, this study reports the development of luminescent and stimuli-responsive Mn^{II} complexes based on the decoration of secondary coordination spheres via a mechanochemical method, which offers an efficient alternative to conventional solution-based synthesis. The introduction of steric bulk and functional groups into the secondary coordination sphere significantly enhanced luminescence efficiency and enabled the synthesized complex to exhibit stimuli-responsive behavior, including thermochromic luminescence. Notably, **Mn-*o*Tol** and Form-II of **Mn-*o*An** exhibit excellent quantum yields of 0.86 and 0.78, respectively. Although a recent study also demonstrated high quantum yields in Mn^{II} complexes using bulky ligands,[6e] the present work is remarkable in achieving similarly high efficiency through a much simpler *ortho*-substitution strategy. Furthermore, Form-I and II of **Mn-*o*An** show unique thermochromic luminescence due to an intramolecular Mn···O interaction. The literature contains very limited reports on Mn^{II} complexes with drastic and reversible thermochromic luminescence, mostly involving phase transitions or competitive emission between two distinct emissive moieties,[4a,18] indicating the need for a systematic molecular design strategy to realize such responsive behavior. Therefore, the proposed strategy involving the modification of the secondary coordination sphere is particularly important, as it is expected to serve as an effective molecular design principle for developing Mn^{II} complexes with stimuli-responsive properties, including thermochromic luminescence. These findings highlight the potential of secondary coordination-sphere engineering as a versatile strategy for designing advanced luminescent materials. Moreover, this work expands the scope of Mn^{II} complexes to encompass optoelectronic applications and smart stimuli-responsive functional "soft crystals."[19] Studies attempting the synthesis and properties of photofunctional Mn^{II} complexes are currently ongoing.

4. Experimental Section

Materials: ***Caution!*** *Although no difficulties are experienced, all the chemicals used in this study are potentially harmful and should be used in small quantities and handled with care in a fume hood.*

$MnBr_2$ and all solvents were purchased from Kishida Chemical Co. Ltd. $MnBr_2{\cdot}4H_2O$ was purchased from Sigma-Aldrich Co. Triphenylphosphine oxide ($OPPh_3$),[14] tri(*o*-tolyl)phosphine oxide ($OP(o\text{-}Tol)_3$),[14] tri(*p*-tolyl)phosphine oxide ($OP(p\text{-}Tol)_3$),[20a] tri(*o*-anisyl)phosphine oxide ($OP(o\text{-}An)_3$),[20b] and $[MnBr_2(OPPh_3)_2]$ (**Mn-Ph**)[3] were synthesized according to the literature.

General Procedure for Mechanochemical Synthesis of Mn-oTol, Mn-pTol, and Mn-Ph: $MnBr_2$ and phosphine oxide (≈2 equiv. based on $MnBr_2$) were manually ground using a mortar and pestle for homogenization. Subsequently, 2–3 drops of EtOH were added to the mixture, which was ground for 5 min; if necessary, this process was repeated until the raw materials completely disappeared. The obtained powder was washed with ethyl acetate under sonication, collected via suction filtration, and dried in vacuo.

Mn-oTol: On reacting $MnBr_2$ (75.0 mg; 0.35 mmol) with $OP(o\text{-}Tol)_3$ (230 mg; 0.72 mmol), the product was obtained as a pale green powder. Yield, 262 mg (0.31 mmol, 88%). Elemental analysis calculated (%) for $C_{42}H_{42}Br_2MnO_2P_2$: C 58.97, H 4.95; Found: C 58.77, H 4.95.

Mn-pTol: On reacting $MnBr_2$ (64.1 mg; 0.30 mmol) with $OP(p\text{-}Tol)_3$ (202 mg; 0.63 mmol), the product was obtained as a pale green powder.

Yield, 206 mg (0.24 mmol, 81%). Elemental analysis calculated (%) for $C_{42}H_{42}Br_2MnO_2P_2$: C 58.97, H 4.95; Found: C 58.79, H 4.78.

Mn-Ph: On reacting $MnBr_2$ (22.6 mg; 0.11 mmol) with $OPPh_3$ (58.8 mg; 0.21 mmol), the product was obtained as a pale green powder. Yield, 54.4 mg (0.071 mmol, 65%). Elemental analysis calculated (%) for $C_{42}H_{42}Br_2MnO_2P_2$: C 56.06, H 3.92; Found: C 55.82, H 3.97.

General Procedure for Conventional Solution-state Synthesis of Mn-oTol and Mn-pTol: A solution containing $MnBr_2$ (0.1 mmol) and phosphine oxide (0.26 mmol) in EtOH (20 mL) was stirred at 60 °C for 1 h and then filtered. The filtrate was concentrated by natural evaporation at ambient temperature (ca. 20 °C) overnight. The resulting residue was washed with EtOAc under sonication and recrystallized from EtOH/Et_2O. The resultant pale green crystals were collected via filtration, washed with Et_2O, and dried in vacuo.

Mn-oTol: Although the synthesis of **Mn-*o*Tol** from the ligand precursor P(*o*-Tol)$_3$ via a one-pot reaction has been reported recently,[8] a synthetic approach using an isolated OP(*o*-Tol)$_3$ ligand was used to synthesize **Mn-*o*Tol** in this study. On reacting $MnBr_2$ (22.2 mg; 0.103 mmol) with OP(*o*-Tol)$_3$ (85.2 mg; 0.266 mmol), pale green crystals of the product were obtained. Yield, 64.3 mg (0.075 mmol, 73%). Single crystals of **Mn-*o*Tol** were prepared by the slow vapor diffusion of Et_2O into a solution of **Mn-*o*Tol** in EtOH in a refrigerator. Elemental analysis calculated (%) for $C_{42}H_{42}Br_2MnO_2P_2$: C 58.97, H 4.95; Found: C 59.06, H 4.93. M.p.: 309 °C (decomp.).

Mn-pTol: On reacting $MnBr_2$ (22.2 mg; 0.103 mmol) with OP(*p*-Tol)$_3$ (84.2 mg; 0.263 mmol), pale green crystals of the product were obtained. Yield, 45.5 mg (0.053 mmol, 51%). Single crystals of **Mn-*p*Tol** were prepared by the slow vapor diffusion of Et_2O into a solution of **Mn-*p*Tol** in EtOH in a refrigerator. Elemental analysis calculated (%) for $C_{42}H_{42}Br_2MnO_2P_2$: C 58.97, H 4.95; Found: C 58.80, H 4.86. M.p.: 265 °C (decomp.).

Synthesis of Mn-oAn—Mechanochemical Synthesis: $MnBr_2$ (67.4 mg, 0.31 mmol) and OP(*o*-An)$_3$ (258 mg, 0.70 mmol) were manually ground using a mortar and pestle for homogenization. After adding 2–3 drops of acetone to the mixture and grinding for 5 min, 2–3 drops of EtOH were added to the mixture, which was ground for 5 min more. The obtained powder (Form-I of **Mn-*o*An**) was washed with ethyl acetate under sonication, collected via suction filtration, and dried in vacuo. Yield, 267 mg (0.28 mmol, 88%). Elemental analysis calculated (%) for $C_{42}H_{42}Br_2MnO_8P_2$: C 53.02, H 4.45; Found: C 53.20, H 4.56. Further grinding the Form-I powder with 4–5 drops of EtOH for 15 min yielded the Form-II powder; if necessary, this process was repeated until the transformation was complete.

Solution-State Synthesis: $MnBr_2$ (46.2 mg, 0.22 mmol) and OP(*o*-An)$_3$ (221 mg, 0.60 mmol) were suspended in acetone (20 mL) and kept at ambient temperature (≈20 °C) overnight. The resulting white suspension of **Mn-*o*An**·acetone was collected by filtration, washed with ethyl acetate and Et_2O, and dried in vacuo. Yield, 196 mg (0.19 mmol, 86%). Single crystals of **Mn-*o*An**·acetone were directly obtained from the reaction solution. Single crystals of **Mn-*o*An** (Form-I and -II) were prepared by the slow vapor diffusion of Et_2O into a solution of **Mn-*o*An** in EtOH under two different conditions. Form-I was obtained by heating an EtOH suspension of **Mn-*o*An** in a 50 °C water bath for a short time (for dissolution) followed by the diffusion of diethyl ether vapor. Form-II was obtained by diffusing diethyl ether vapor into a firmly dissolved EtOH solution of **Mn-*o*An** in a refrigerator for several days. Elemental analysis calculated (%) for $C_{42}H_{42}Br_2MnO_8P_2$: C 53.02, H 4.45; Found: C 52.91, H 4.38. M.p.: 211 °C (decomp.).

Apparatus—Single-Crystal X-Ray Structural Analysis: Although the crystal structure of **Mn-*o*Tol** is previously reported,[8] to enable structural comparison under identical conditions, **Mn-*o*Tol** was structurally characterized along with the other Mn^{II} complexes in this study. All single crystal X-ray diffraction measurements were performed using a Rigaku XtaLAB-Synergy diffractometer with a HyPix-6000HE area detector and a multilayer mirror-monochromated Cu K_α radiation (λ = 1.54184 Å). Each crystal was mounted on a MicroMount using liquid paraffin and cooled by an N_2-flow type temperature controller. Diffraction data were collected and processed using *CrysAlisPro*.[21] The structures were solved using *SHELXT-2018*[22] by the intrinsic phasing method. Structure refinements were conducted by the full-matrix least squares techniques with *SHELXL-2018*.[23] All non-hydrogen atoms were refined anisotropically, and the hydrogen atoms were refined using the riding model. Molecular graphics were generated using *ORTEP-3*[24a] and *POV-RAY*.[24b] The crystallographic data and the selected interatomic distances and angles are listed in Tables S1 and S2 (Supporting Information). Full crystallographic data have been deposited with the Cambridge Crystallographic Data Centre (CCDC 2449475–2449481).

Luminescence Measurements: The measurements were conducted in an air-conditioned room maintained at ≈20 °C and a relative humidity of ≈ 30%, as the emission properties are sensitive to moisture. Emission spectra were acquired using a JASCO FP-8600 spectrometer. Emission quantum yields were recorded using a Hamamatsu Photonics C9920-02 absolute photoluminescence quantum yield measurement system equipped with an integrating sphere apparatus and a 150 W CW xenon light source. The accuracy of the instrument was confirmed by measuring the quantum yield of anthracene in ethanol (Φ = 0.27).[25] Emission lifetime measurements were conducted using a Hamamatsu Photonics Quantaurus-Tau C11367 fluorescence lifetime spectrometer equipped with a xenon flash light source (60 W). The emission decay was analyzed using a single exponential function. For the variable-temperature emission measurements, a liquid N_2 cryostat (UNISOKU CoolSpeK USP203-C) was used to control the sample temperature.

Water Vapor-Exposure Experiments: The samples were dried at 110 °C for 30 min and cooled under vacuum before exposure to water vapor. A small amount of the sample was placed in a quartz glass tube, which was then placed in a capped glass vial containing a small amount of saturated aqueous solution of various metal salts (to control the RH).[26] The vial was kept in a temperature-controlled incubator at 293 K for two days. The quartz tube was capped before measurement to maintain each sample at the corresponding RH.

Other Measurements: Powder X-ray diffraction (PXRD) measurements were conducted using Cu K_α radiation (λ = 1.5418 Å) on a Rigaku MiniFlex600 diffractometer or a Bruker D2 Phaser diffractometer. UV–vis absorption spectra were recorded on a Shimadzu UV-2500 PC spectrophotometer. UV–vis diffuse reflectance spectra were recorded on a JASCO V-670 spectrophotometer equipped with an integrating sphere apparatus, and the measured reflectivity was converted using the Kubelka–Munk function. Thermogravimetric-differential thermal analyses (TG-DTA) were conducted on a Rigaku Thermoplus EVO2 TG-DTA 8122 under Ar flow (0.1 L min^{-1}). Optical microscopic observations were conducted using a KEYENCE VHX-6000 digital microscope equipped with a LINKAM THMS600 heating/freezing stage. Magnetic measurements were carried out using a Quantum-Design MPMS XL7AC SQUID magnetometer. The observed magnetic moment data were corrected for the diamagnetic contribution (χ_{dia}) by the equation: $\chi_{dia} = -1/2 \times M \times 10^{-6}$ cm^3 mol^{-1}. Elemental analysis was carried out on the J-SCIENCE LAB JM-11 elemental analyzer at the Organic Microanalysis Laboratory at Kyoto University.[27–29]

Supporting Information

Supporting Information is available from the Wiley Online Library or from the author.

Acknowledgements

M.Y. and F.Z. are Co-first authors. This work was supported by the JSPS KAKENHI, grant numbers JP21K05094, JP22H02098, JP23K23366, and JP24K08455, as well as by the Hyogo Science and Technology Association (5079) and the Kyoto Technoscience Center. The magnetic measurement was performed at the Analytical Instrument Facility, Graduate School of Science, the University of Osaka.

Conflict of Interest

The authors declare no conflict of interest.

Data Availability Statement

The data that support the findings of this study are available in the supplementary material of this article.

Keywords

crystal structure, luminescence, mechanochemical synthesis, Mn complex, thermochromism

Received: June 23, 2025
Revised: August 4, 2025
Published online:

[1] a) N. Armaroli, *Chem. Soc. Rev.* **2001**, *30*, 113; b) A. Kobayashi, M. Kato, *Chem. Lett.* **2017**, *46*, 154; c) O. S. Wenger, *J. Am. Chem. Soc.* **2018**, *140*, 13522; d) C. Förster, K. Heinze, *Chem. Soc. Rev.* **2020**, *49*, 1057; e) C. Wegeberg, O. S. Wenger, *JACS Au* **2021**, *1*, 1860; f) H. Takeda, A. Kobayashi, K. Tsuge, *Coord. Chem. Rev.* **2022**, *470*, 214700; g) N. Sinha, O. S. Wenger, *J. Am. Chem. Soc.* **2023**, *145*, 4903; h) M. Kato, *Adv. Inorg. Chem.* **2024**, *83*, 33.

[2] a) Q. Zhou, L. Dolgov, A. M. Srivastava, L. Zhou, Z. Wang, J. Shi, M. D. Dramićanin, M. G. Brik, M. Wu, *J. Mater. Chem. C* **2018**, *6*, 2652; b) Y. Qin, P. She, X. Huang, W. Huang, Q. Zhao, *Coord. Chem. Rev.* **2020**, *416*, 213331; c) P. Tao, S.-J. Liu, W.-Y. Wong, *Adv. Opt. Mater.* **2020**, *8*, 2000985; d) D. Liang, H. Xiao, W. Cai, S. Lu, S. Zhao, Z. Zang, L. Xie, *Adv. Opt. Mater.* **2023**, *11*, 2202997; e) W. Zhang, W. Zheng, L. Li, P. Huang, J. Xu, W. Zhang, Z. Shao, X. Chen, *Adv. Mater.* **2024**, *36*, 2408777.

[3] a) D. M. L. Goodgame, F. A. Cotton, *J. Chem. Soc.* **1961**, 3735; b) F. A. Cotton, L. M. Daniels, P. Huang, *Inorg. Chem.* **2001**, *40*, 3576.

[4] a) Y. Wu, X. Zhang, Y.-Q. Zhang, M. Yang, Z.-N. Chen, *Chem. Commun.* **2018**, *54*, 13961; b) M. Bortoluzzi, J. Castro, A. Gobbo, V. Ferraro, L. Pietrobon, *Dalton Trans.* **2020**, *49*, 7525; c) M. Bortoluzzi, J. Castro, A. Di Vera, A. Palù, V. Ferraro, *New J. Chem.* **2021**, *45*, 12871; d) X. Huang, Y. Qin, P. She, H. Meng, S. Liu, Q. Zhao, *Dalton Trans.* **2021**, *50*, 8831; e) A. V. Artem'ev, M. P. Davydova, A. S. Berezin, T. S. Sukhikh, D. G. Samsonenko, *Inorg. Chem. Front.* **2021**, *8*, 2261; f) D.-H. Kong, Y. Wu, C.-M. Shi, H. Zeng, L.-J. Xu, Z.-N. Chen, *Chem. Sci.* **2024**, *15*, 16698; g) X. Zheng, Z. Zhou, Z. Li, K.-Y. Tran, P. She, H. Wang, W.-Y. Wong, Q. Zhao, P. Tao, *J. Mater. Chem. C* **2024**, *12*, 8296.

[5] a) M. Bortoluzzi, J. Castro, E. Trave, D. Dallan, S. Favaretto, *Inorg. Chem. Commun.* **2018**, *90*, 105; b) M. P. Davydova, I. A. Bauer, V. K. Brel, M. I. Rakhmanova, I. Yu Bagryanskaya, A. V. Artem'ev, *Eur. J. Inorg. Chem.* **2020**, *2020*, 695; c) A. V. Artem'ev, M. P. Davydova, A. S. Berezin, V. K. Brel, V. P. Morgalyuk, I. Yu Bagryanskaya, D. G. Samsonenko, *Dalton Trans.* **2019**, *48*, 16448, d) H. Meng, W. Zhu, F. Li, X. Huang, Y. Qin, S. Liu, Y. (M.) Yang, W. Huang, Q. Zhao, *Laser Photon. Rev.* **2021**, *15*, 2100309; e) Z. Zhou, T. Jiang, Y. Yang, Y. Deng, M. Wang, Y. Ma, S. Liu, Q. Zhao, *Adv. Opt. Mater.* **2024**, *12*, 2302185.

[6] a) J. Chen, Q. Zhang, F.-K. Zheng, Z.-F. Liu, S.-H. Wang, A-Q. Wu, G.-C. Guo, *Dalton Trans.* **2015**, *44*, 3289; b) Y. Qin, P. Tao, L. Gao, P. She, S. Liu, X. Li, F. Li, H. Wang, Q. Zhao, Y. Miao, W. Huang, *Adv. Opt. Mater.* **2019**, *7*, 1801160; c) A. V. Artem'ev, M. P. Davydova, M. I. Rakhmanova, I. Yu Bagryanskaya, D. P. Pishchur, *Inorg. Chem. Front.* **2021**, *8*, 3767; d) G.-H. Tan, Y.-N. Chen, Y.-T. Chuang, H.-C. Lin, C.-A. Hsieh, Y.-S. Chen, T.-Y. Lee, W.-C. Miao, H.-C. Kuo, L.-Y. Chen, K.-T. Wong, H.-W. Lin, *Small* **2023**, *19*, 2205981; e) P. She, Z. Zheng, Y. Qin, F. Li, X. Zheng, D. Zhang, Z. Xie, L. Duan, W.-Y. Wong, *Adv. Opt. Mater.* **2024**, *12*, 2302132; f) Z.-Z. Huo, Y. Wang, B. Yang, J.-Q. Liang, X.-F. Hong, Q. An, L. Yuan, H. Ma, J.-L. Zuo, Y.-X. Zheng, *Adv. Opt. Mater.* **2025**, *13*, 2402684.

[7] a) V. Morad, I. Cherniukh, L. Pöttschacher, Y. Shynkarenko, S. Yakunin, M. V. Kovalenko, *Chem. Mater.* **2019**, *31*, 10161; b) L. Mao, P. Guo, S. Wang, A. K. Cheetham, R. Seshadri, *J. Am. Chem. Soc.* **2020**, *142*, 13582; c) V. Sääsk, Y.-A. Chen, T.-F. Huang, L.-Y. Ting, T.-A. Luo, S. Fujii, K. Põhako-Esko, M. Yoshida, M. Kato, T.-L. Wu, H.-H. Chou, *Eur. J. Inorg. Chem.* **2024**, *27*, 202300562.

[8] J. Lu, J. Gao, S. Wang, M.-J. Xie, B.-Y. Li, W.-F. Wang, J.-R. Mi, F.-K. Zheng, G.-C. Guo, *Nano Lett.* **2023**, *23*, 4351.

[9] a) S. L. James, C. J. Adams, C. Bolm, D. Braga, P. Collier, T. Friščić, F. Grepioni, K. D. M. Harris, G. Hyett, W. Jones, A. Krebs, J. Mack, L. Maini, A. G. Orpen, I. P. Parkin, W. C. Shearouse, J. W. Steed, D. C. Waddell, *Chem. Soc. Rev.* **2012**, *41*, 413; b) M. Leonardi, M. Villacampa, J. C. Menéndez, *Chem. Sci.* **2018**, *9*, 2042; c) K. Kubota, H. Ito, *Trends Chem* **2020**, *2*, 1066; d) B. Szczęśniak, S. Borysiuk, J. Choma, M. Jaroniec, *Mater. Horiz.* **2020**, *7*, 1457.

[10] a) H. Ohara, A. Kobayashi, M. Kato, *Chem. Lett.* **2014**, *43*, 1324; b) A. Kobayashi, T. Hasegawa, M. Yoshida, M. Kato, *Inorg. Chem.* **2016**, *55*, 1978; c) P. Liang, A. Kobayashi, T. Hasegawa, M. Yoshida, M. Kato, *Eur. J. Inorg. Chem.* **2017**, *2017*, 5134.

[11] E. O. Wollan, W. C. Koehler, M. K. Wilkinson, *Phys. Rev.* **1958**, *110*, 638.

[12] a) H. Ohtsu, M. Kawano, *Chem. Commun.* **2017**, *53*, 8818; b) M. Kawano, T. Haneda, D. Hashizume, F. Izumi, M. Fujita, *Angew. Chem., Int. Ed.* **2008**, *47*, 1269; c) H. Ito, M. Muromoto, S. Kurenuma, S. Ishizaka, N. Kitamura, H. Sato, T. Seki, *Nat. Commun.* **2013**, *4*, 2009.

[13] a) A. Jana, S. Zhumagali, Q. Ba, A. S. Nissimagoudar, K. S. Kim, *J. Mater. Chem. A* **2019**, *7*, 26504; b) H. Peng, B. Zou, Y. Guo, Y. Xiao, R. Zhi, X. Fan, M. Zou, J. Wang, *J. Mater. Chem. C* **2020**, *8*, 6488; c) A. Ben-Akacha, C. Zhou, M. Chaaban, D. Beery, S. Lee, M. Worku, X. Lin, R. Westphal, B. Ma, *ChemPhotoChem* **2021**, *5*, 326; d) Y.-Y. Ma, Y.-R. Song, W.-J. Xu, Q.-Q. Zhong, H.-Q. Fu, X.-L. Liu, C.-Y. Yue, X.-W. Lei, *J. Mater. Chem. C* **2021**, *9*, 9952; e) H. Tang, Y. Xu, X. Hu, H. Chen, S. Wang, W. Jiang, Q. Hu, L. Wang, W. Jiang, *Laser Photon. Rev.* **2024**, *18*, 2300672.

[14] S. Jena, A. T. M. Munthasir, P. Thilagar, *J. Mater. Chem. C* **2022**, *10*, 9124.

[15] U. Lanver, G. Lehmann, *J. Lumin* **1978**, *17*, 225.

[16] a) Y. Wu, X. Zhang, L.-J. Xu, M. Yang, Z.-N. Chen, *Inorg. Chem.* **2018**, *57*, 9175; b) C. Jiang, Q. Luo, C. Luo, H. Lin, H. Peng, *J. Phys.: Condens. Matter.* **2022**, *34*, 154001; c) W. Ma, Q. Qian, S. M. H. Qaid, S. Zhao, D. Liang, W. Cai, Z. Zang, *Nano Lett.* **2023**, *23*, 8932; d) Z. Huang, Y. Wang, P. Du, W. Gao, P. Niu, D. Xu, L. Wang, Y. Deng, A. Song, *Inorg. Chem.* **2024**, *63*, 21059; e) Y. Wu, X. Zhang, B. Zhang, L.-D. Xin, X.-M. Zhen, L.-J. Xu, *J. Mater. Chem. C* **2024**, *12*, 16471.

[17] a) M. Bortoluzzi, J. Castro, F. Enrichi, A. Vomiero, M. Busato, W. Huang, *Inorg. Chem. Commun.* **2018**, *92*, 145; b) M. Bortoluzzi, J. Castro, A. Gobbo, V. Ferraro, L. Pietrobon, S. Antoniutti, *New J. Chem.* **2020**, *44*, 571; c) M. Bortoluzzi, V. Ferraro, J. Castro, *Dalton Trans.* **2021**, *50*, 3132; d) X. Zheng, P. Tao, H. Wang, W.-Y. Wong, *ACS Appl. Opt. Mater.* **2025**, *3*, 942; e) X. Zheng, P. Tao, H. Wang, L. Zhang, W.-Y. Wong, *J. Inorg. Organomet. Polym.* **2025**, https://doi.org/10.1007/s10904-025-03794-5; f) M. P. Davydova, I. Yu Bagryanskaya, I. A. Bauer, M. I. Rakhmanova, V. P. Morgalyuk, V. K. Brel, A. V. Artem'ev, *Polyhedron* **2020**, *188*, 114706; g) M. Bortoluzzi, J. Castro, V. Ferraro, *Inorg. Chim. Acta* **2022**, *536*, 120896; h) M. P. Davydova, L. Meng, M. I. Rakhmanova, Z. Jia, A. S. Berezin, I. Yu Bagryanskaya, Q. Lin, H. Meng, A. V. Artem'ev, *Adv. Mater.* **2023**, *35*, 2303611; i) V. Ferraro, J. Castro, L. Agostinis, M. Bortoluzzi, *Inorg. Chim. Acta* **2023**, *545*, 121285; j) V. Ferraro, J. Castro, M. Bortoluzzi, *Molecules* **2024**, *29*, 239.

[18] a) A. S. Berezin, D. G. Samsonenko, V. K. Brelc, A. V. Artem'ev, *Dalton Trans.* **2018**, *47*, 7306; b) W. Shen, S. Sui, W. Yuan, A. Wang, Y. Tao, S. Chen, Z. Deng, *J. Mater. Chem. C* **2021**, *9*, 2729; c) Z.-L. He, J.-H. Wei, J.-B. Luo, Z.-Z. Zhang, D.-B. Kuang, *J. Mater. Chem. C* **2023**, *11*,

1251; d) G.-H. Tan, H.-C. Lin, H.-C. Liang, C.-W. Pao, P.-Y. Chen, W.-T. Chuang, C.-A. Hsieh, D. M. Dorrah, M.-C. Li, L.-Y. Chen, H.-H. Chou, H.-W. Lin, *ACS Appl. Mater. Interfaces* **2024**, *16*, 55842; e) W. Lv, Y. Tang, C. Han, Z. Miao, C. Sun, L. Xu, G. Wu, Z. Liu, Y. Tao, R. Chen, *Inorg. Chem.* **2025**, *64*, 11032; f) Z. Huang, X. Wang, P. Du, C. Feng, P. Niu, D. Xu, L. Wang, W. Gao, A. Song, *Inorg. Chem.* **2025**, *64*, 31000; g) A. V. Artem'ev, M. P. Davydova, A. S. Berezin, D. G. Samsonenko, I. Yu Bagryanskaya, V. K. Brel, X. Hei, K. A. Brylev, O. I. Artyushin, L. E. Zelenkov, I. I. Shishkin, J. Li, *ACS Appl. Mater. Interfaces* **2022**, *14*, 31000.

[19] a) M. Kato, H. Ito, M. Hasegawa, K. Ishii, *Chem.-Eur. J.* **2019**, *25*, 5105; b) M. Kato, M. Yoshida, Y. Sun, A. Kobayashi, *J. Photochem. Photobiol. C* **2022**, *51*, 100477.

[20] a) Y. Hasegawa, T. Ohkubo, T. Nakanishi, A. Kobayashi, M. Kato, T. Seki, H. Ito, K. Fushimi, *Eur. J. Inorg. Chem.* **2013**, *2023*, 5911; b) Y. Kitagawa, S. Wada, M. D. J. Islam, K. Saita, M. Gon, K. Fushimi, K. Tanaka, S. Maeda, Y. Hasegawa, *Commun. Chem.* **2020**, *3*, 119.

[21] CrysAlisPro, Rigaku Corporation, Tokyo, Japan, **2015**.

[22] G. M. Sheldrick, *Acta Crystallogr., Sect. A: Found. Crystallogr.* **2015**, *71*, 3.

[23] G. M. Sheldrick, *Acta Crystallogr. Sect. C* **2015**, *71*, 3.

[24] a) L. J. Farrugia, *J. Appl. Crystallogr.* **1997**, *30*, 565; b) T. D. Fenn, D. Ringe, G. A. Petsko, *J. Appl. Crystallogr.* **2003**, *36*, 944.

[25] a) W. R. Dawson, M. W. Windsor, *J. Phys. Chem.* **1968**, *72*, 3251; b) W. H. Melhuish, *J. Phys. Chem.* **1961**, *65*, 229.

[26] H. L. Goderis, B. L. Fouwe, S. M. Van Cauwenbergh, P. P. Tobback, *Anal. Chem.* **1986**, *58*, 1561.

[27] K. Sudarsanan, *Acta Crystallogr. Sect. B* **1975**, *31*, 2720.

[28] K. Momma, F. Izumi, *J. Appl. Cryst.* **2011**, *44*, 1272.

[29] C. A. Parker, W. T. Rees, *Analyst* **1960**, *85*, 587.